A computational and experimental approach to understanding material flow behavior during additive friction stir deposition (AFSD)

Stubblefield, G. G.; Fraser, K. A.; Robinson, T. W.; Zhu, N.; Kinser, R. P.; Tew, J. Z.; Cordle, B. T.; Jordon, J. B.; Allison, P. G.

Publisher's version / Version de l'éditeur:
https://doi.org/10.1007/s40571-023-00578-x
Computational Particle Mechanics, 2023-04-19

Computational Particle Mechanics
https://doi.org/10.1007/s40571-023-00578-x

A computational and experimental approach to understanding material flow behavior during additive friction stir deposition (AFSD)

G. G. Stubblefield[1] · K. A. Fraser[2] · T. W. Robinson[3] · N. Zhu[4,5] · R. P. Kinser[4,5] · J. Z. Tew[3] · B. T. Cordle[3] · J. B. Jordon[4,5] · P. G. Allison[4,5]

Received: 13 October 2022 / Revised: 22 February 2023 / Accepted: 28 February 2023

Abstract
In this study, a combined computational and experimental particle tracking investigation was performed for a solid-state additive manufacturing and repair process, Additive Friction Stir Deposition (AFSD). Specifically, smoothed particle hydrodynamics (SPH) simulations of AFSD were conducted in-order to elucidate deposition mechanics. The particle tracking of the SPH AFSD simulations was validated using experimental depositions of two feedstock varieties, including anodized AA6061-T6 feedstock to track external particles and AA6061-T6 copper wire core feedstock to track internal particles, to represent flow behavior from different regions of the feedstock. The X-Ray computed tomography (CT) experimental results revealed that the anodized oxides on the outside of the feedstock flowed to the retreating side, whereas the copper wire in the center of the feedstock migrated to the advancing side. Particle tracking results from the SPH simulations showed that, in general, particle movement is limited to directly beneath the feedstock. The rotational, radial, and traverse flow interactions visualized by AFSD simulations explained the advancing and retreating side biases experienced by the internal copper wire and surface oxides on the anodized feedstock. This work demonstrates the ability to predict AFSD material distributions, which has a significant impact on as-deposited material quality.

✉ P. G. Allison
Paul_Allison@Baylor.edu

[1] Geotechnical and Structures Lab, U.S. Army Engineer Research and Development Center, Vicksburg, MS, USA

[2] National Research Council Canada, Saguenay, QC, Canada

[3] Mechanical Engineering Department, The University of Alabama, Tuscaloosa, AL, USA

[4] Mechanical Engineering Department, Baylor University, Waco, TX, USA

[5] Point-of-Need Innovations (PONI) Center, Baylor University, Waco, TX, USA

Published online: 19 April 2023

Graphical abstract

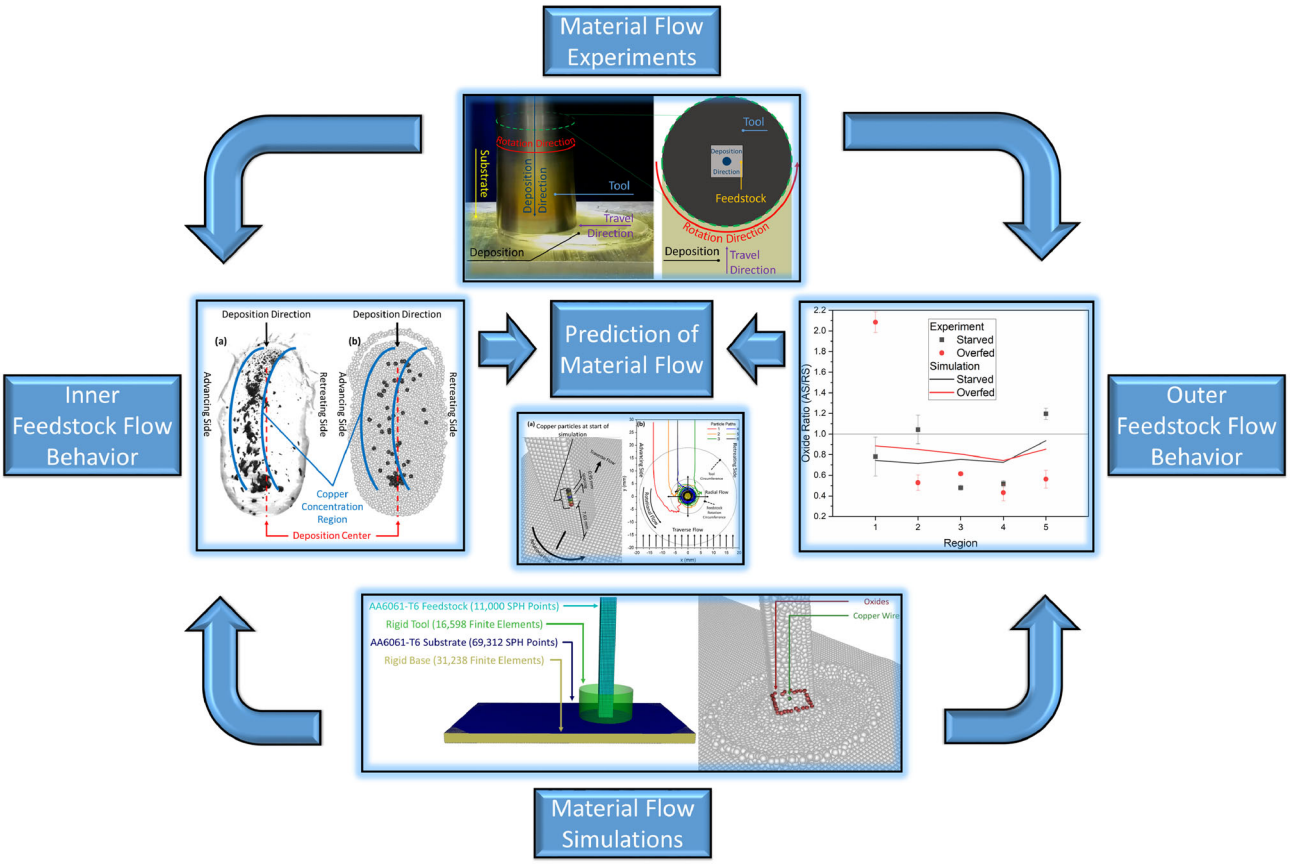

Keywords Additive friction stir deposition · Oxides · Smooth particle hydrodynamics · Severe plastic deformation · Particle tracking · Material flow

1 Introduction

Non-fusion-based additive manufacturing and repair techniques provide a complementary approach where melting of the feedstock is undesirable when lower heat inputs may be necessary to minimize residual stress and distortion in substrates and/or builds [1–3], or where a necessary microstructure may be required [4–6]. One solid-state technique gaining attention from the community, Additive Friction Stir Deposition (AFSD), depicted in Fig. 1, is a nascent solid-state additive manufacturing and repair process, where the solid-state attribute refers to limiting processing temperature below the melting point, as opposed to fusion-based processes that exceed the melting point.

During the AFSD process, feedstock material is deposited through the square hole of a rotating tool onto a substrate or subsequent layers. The rotating tool generates frictional heat, which softens the feedstock material to facilitate material flow outwards while traveling forward to leave behind a plasticized layer of material. The rotating tool shoulder has been observed to break up surface oxides on the feedstock and substrate to create metallurgical bonds between the deposition and substrate [7]. Considerable research has been contributed toward AFSD in areas such as mechanical properties [8–15], machine learning [16], output microstructure [17–22], recycling material [23], repair capabilities [24], and processing temperature [25]. However, understanding material flow of deposited material, and especially of oxides, which may be difficult to remove from secondary feedstocks such as waste material in remote locations where the AFSD technique is gaining considerable interest for point-of-need manufacturing.

It is well understood by the scientific community that metals can form surface oxides that must either be removed or broken up to facilitate metallurgical bonding [26]. Typically, in Friction Stir Welding (FSW), the severe plastic deformation induced by the spinning tool breaks up the oxide films into smaller oxide particles, which are then trapped within the

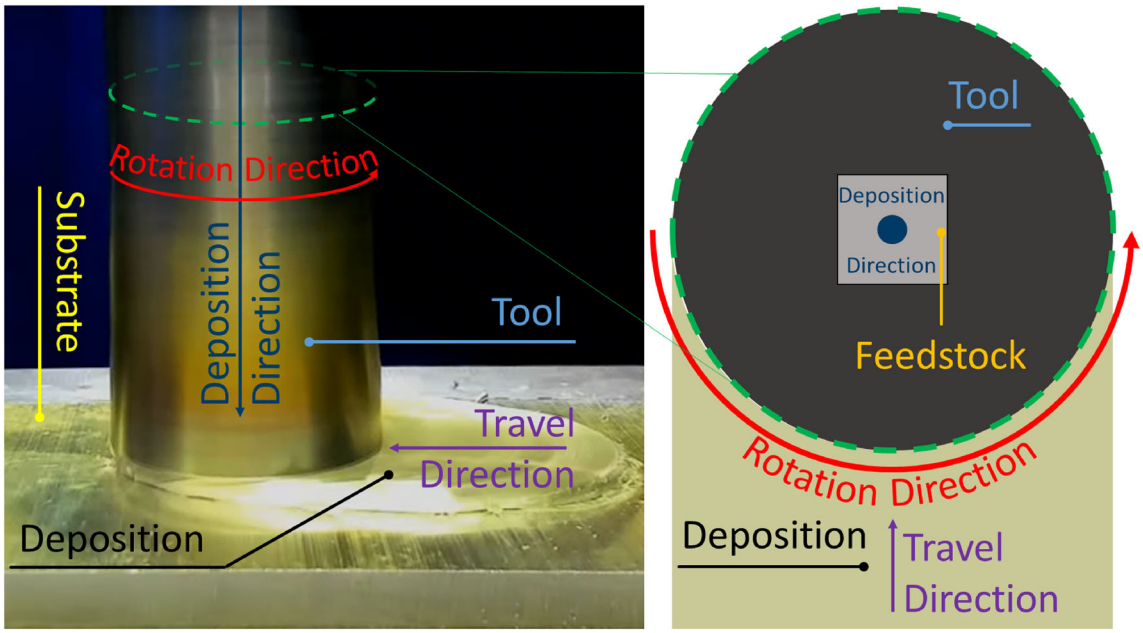

Fig. 1 Description of AFSD process where a feedstock material is pushed through a spinning non-consumable tool onto a substrate

joined material [27]. However, poor processing parameters, which result in weak material flow, may fail to adequately break up the oxide film, resulting in kissing bonds or the lazy "s" feature [28–32]. These features may act as stress concentrations and crack nucleation sites within the FSW, which decrease fatigue performance [33, 34]. The oxide problem compounds when considering that oxide type defects are also difficult to detect without destructive testing [35]. Given the importance of oxide distribution in FSW plates, FSW tool manufacturers are particularly interested in oxide movement during FSW.

One solution to understanding the oxide problem in FSW is to utilize particle tracking simulations. Specifically, researchers have used particle tracking simulations in FSW to study material flow in the stir zone [36, 37]. FSW material flow behavior is beneficial to study, since the flow largely determines the finished weld bond strength, material homogeneity, weld asymmetry, and defect formation. One study by Fraser et al. used FSW simulations, validated by X-Ray computed tomography (XRCT), to identify wormhole defects in the stir zone of FSW [38]. Another study by Dialami et al. used FSW foil marker experiments in concert with simulations to visualize the lazy "s" feature formation in the weld nugget [39].

Given the deleterious effects oxides have on FSW parts, and the ability of particle tracking simulations to help understand the oxide problems, similar particle tracking of AFSD simulation studies needs to be conducted to improve AFSD part quality. While most of the AFSD research to-date has focused on the materials science and mechanical performance side of AFSD, limited studies have been carried out on the simulation of AFSD [40, 41]. The smoothed particle hydrodynamics (SPH) simulations previously developed by Stubblefield et al. [40, 41] provide the framework for particle tracking simulations. SPH is a prime candidate for particle tracking simulations, because SPH simulations naturally discretize the domain into smaller material points.

This study aims to explore AFSD particle tracking simulations to elucidate how feedstock material flows during the AFSD process. Two different types of experimental AFSD depositions were used for model calibration: anodized AA6061 rod feedstock with surface oxides to examine outer particle movement and AA6061 feedstock with copper wire cores to track material/particles from the center of the feedstock during deposition. The anodized feedstock rods contained a thick oxide layer, which, when deposited, resulted in the dispersal of aluminum oxides throughout the depositions. Optical microscopy was employed to quantify the surface area of oxides present in the experimental depositions. The copper wire core feedstock depositions resulted in the dispersal of copper throughout the depositions. XRCT scans mapped the copper distribution within the deposited aluminum matrix. Unique insight into particle flow behavior was also explored for each of the simulations.

2 Materials and methods

2.1 Additive friction stir deposition experiments

2.1.1 Anodized feedstock depositions

Anodized feedstocks were utilized to represent material flow behavior from the outside of the feedstock. The anodized AA6061-T6 feedstock rod depositions have been detailed in a previous study by Ning et al. [7]. Specifically, to create the oxide surface, the feedstock rods were anodized in sulfuric acid resulting in an oxide layer approximately 69 μm thick on the outside of the feedstock. Two different depositions were created with the anodized feedstock rods. The tool rotational speed, traverse speed, and layer height were identical for both studies (300 rpm, 2.12 mm/s, 1.5 mm). To show how actuator feed rate would vary oxide distribution, the actuator feed rate was varied for each deposition. The first deposition, which will be referred to as the starved deposition, used a 1.06 mm/s actuator feed rate, which would result in a part with a narrow deposition width and significant surface galling. The second deposition, which will be referred to as the overfed deposition, used a 4.24 mm/s actuator feed rate, which would result in a part with large deposition width.

2.1.2 Copper wire core deposition

While the anodized oxides represented material flow from the outside of the feedstock, the copper wire in the copper wire core depositions represented material flow from the center of the feedstock. The feedstock, as shown in Fig. 2, was created by cutting a 1 mm wide, 5.76 mm deep channel into a 9.53 mm square 152.4 mm long rod of AA6061-T6. A copper wire was pressed into the channel followed by a 1 mm wide, 4.76 mm tall, and 152.4 mm long piece of AA6061-T6 to fill in the remainder of the channel. For the copper wire core deposition, the tool rotational speed, traverse speed, layer height, and actuator feed rate were 300 rpm, 2.12 mm/s, 1.5 mm, and 2.12 mm/s, respectively.

2.2 Microstructural characterization of depositions

The anodized feedstock samples were sectioned using Mitsubishi MV 1200S wire-cut electrical discharge machine and polished using 1 μm diamond suspension. A Keyence VHX 7100 Microscope was used to create micrographs at 150 × magnification for oxide analysis. A Thermo Fisher Scientific Apreo scanning electron microscope was used to perform energy-dispersive x-ray spectroscopy (EDS) from EDAX to collect compositional information of the oxides at 20 kV and 0.4 nA with a working distance of 10 mm. The copper wire core deposition was analyzed using a North Star Imaging

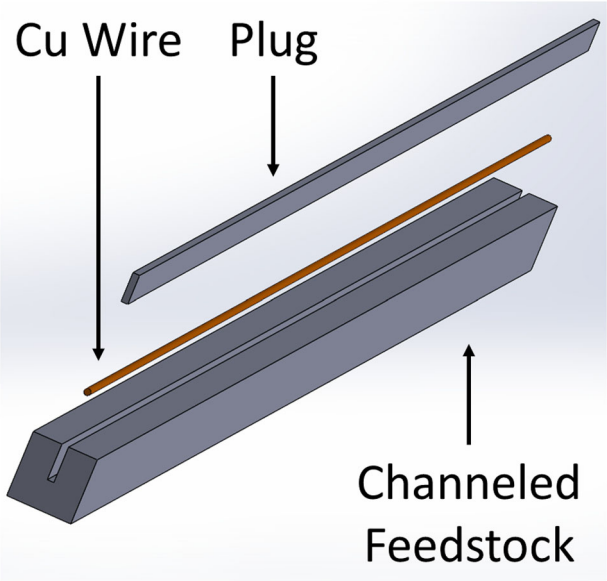

Fig. 2 Feedstock used in copper wire core deposition. After cutting out the channel in the feedstock, the copper wire was inserted into the channel followed by the plug

XRCT machine to highlight copper distributed throughout the AFSD builds.

2.3 SPH methodology

When tasked with computer simulations, most researchers choose the finite element method (FEM) to approximate the governing equations. FEM is a powerful tool for handling problems with nonlinear geometry and complicated boundary conditions. FEM is typically based on the Galerkin method, which is a weighted residual method that approximates governing equations over the entire problem domain with a finite number of shape functions.

The FEM formulation discretizes simulated parts into a series of nodes and geometrical shapes called elements, and the connectivity between nodes and elements is known as the mesh. In contrast, SPH is a collocation method where the governing equations of AFSD are evaluated at a series of material points through the formulation shown in Eq. 1 taken from Liu and Liu 2003 [42].

$$f(x_i) = \sum_{j=1}^{N} \frac{m_j}{\rho_j} f\left(x_j\right) W\left(x_i - x_j, h\right) \tag{1}$$

where $f(x_i)$ is the function to be evaluated at a particle of interest x_i, m_j and ρ_j are the mass and density of the neighboring particle x_j, N is the number of neighbors for the particle of interest x_i, and $W\left(x_i - x_j, h\right)$ is the smoothing function, which is evaluated based on the distance between the particle of interest and the neighboring particle $x_i - x_j$

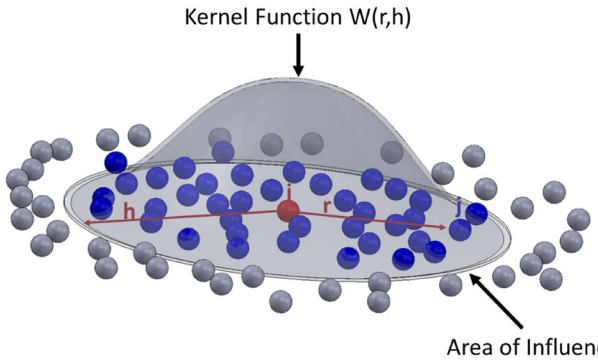

Fig. 3 SPH kernel function illustrating the influence domain of a particle and the neighboring particles that fall under the influence domain [40]

and the smoothing length h, which is multiplied by particle radius to determine how far out the particle influence reaches. An illustration of the SPH method with a particle of interest, kernel (smoothing) function, and neighboring particles is provided in Fig. 3.

Unlike with FEM, the SPH formulation does not include elements to discretize simulated parts, and therefore is known as a meshfree method. The smoothing function used in this study is the hyperbolic spline function taken from Yang et al. [43] and shown in Eqs. 2–3.

$$W(s,\,h) = \alpha_d \begin{cases} s^3 - 6s + 6 \,, & 0 \le s < 1 \\ (2-s)^3 & ,\ 1 \le s < 2 \\ 0 & ,\ s \ge 2 \end{cases} \tag{2}$$

$$s = \frac{x_i - x_j}{h} \tag{3}$$

where α_d is the normalizing factor, which for 3D problems is $15/\left(62\pi h^3\right)$.

For particle tracking purposes, SPH is a natural candidate because SPH uses a Lagrangian reference frame, which provides a history of the movement of each particle over time. Also, SPH is more suitable than a Lagrangian FEM method for tracking particles over severe deformation, because SPH material points represent small particles that freely move within the problem domain, which are not constrained by a predefined mesh. The SPH approximation was applied to a series of continuum mechanics equations shown in [44]. The SPH methodology discretizes PDEs into ODEs, which can then be solved temporally with time integration, a sample of which can be seen in Table 1. Due to the nonlinearity that would arise during severe deformation, the authors in this study used the leapfrog forward difference method to temporally integrate the governing equations.

2.4 AFSD SPH simulations

The simulation model setup is shown in Fig. 4. The SPH code, SPHriction-3D, was initially developed by Fraser [44] for FSW simulations, and was adapted by Stubblefield et al. [40] for AFSD simulations. The substrate was comprised of 69,312 SPH material points with approximately 1 mm spacing. The feedstock was comprised of 11,000 SPH material points with approximately 1 mm spacing. The rigid tool was comprised of 16,598 triangular finite elements with approximately 1 mm spacing. The rigid base was comprised of 31,238 triangular finite elements with approximately 1 mm

Table 1 Sample of PDEs approximated by the SPH method for use in AFSD simulations

Name	PDE	SPH
Conservation of mass	$\frac{D\rho}{Dt} + \rho\nabla\cdot\overline{v} = 0$	$\frac{D\rho_i}{Dt} = \rho_i \sum_{j=1}^{N_i} \frac{m_j}{\rho_j}\left(v_i^\beta - v_j^\beta\right)\frac{\partial W_{ij}}{\partial x_i^\beta}$
Conservation of momentum	$\frac{D\overline{v}}{Dt} = \frac{1}{\rho}\nabla\cdot\overline{\overline{\sigma}}$	$\frac{Dv_i^\alpha}{Dt} = \sum_{j=1}^{N_i} m_j\left(\frac{\sigma_i^{\alpha\beta}}{\rho_i^2} + \frac{\sigma_j^{\alpha\beta}}{\rho_j^2}\right)\frac{\partial W_{ij}}{\partial x_i^\beta}$
Jaumann stress rate	$\frac{\mathrm{d}\overline{\overline{S}}}{\mathrm{d}t} = 2G\left(\dot{\overline{\overline{\varepsilon}}} - \frac{1}{3}tr\left(\dot{\overline{\overline{\varepsilon}}}\right)\overline{\overline{\delta}}\right) + \overline{\overline{S\Omega}}^T + \overline{\overline{\Omega S}}$	$\frac{\mathrm{d}S^{\alpha\beta}}{\mathrm{d}t} = 2G\left(\dot{\varepsilon}^{\alpha\beta} - \frac{1}{3}\delta^{\alpha\beta}\dot{\varepsilon}^{\gamma\gamma}\right) + S^{\alpha\gamma}\Omega^{\beta\gamma} + \Omega^{\alpha\gamma}S^{\gamma\beta}$
Stress decomposition	$\overline{\overline{\sigma}} = \overline{\overline{S}} - p\overline{\overline{\delta}}$	$\sigma_i^{\alpha\beta} = S_i^{\alpha\beta} - p_i\delta^{\alpha\beta}$
Strain rate	$\dot{\overline{\overline{\varepsilon}}} = \frac{1}{2}\left(\nabla^s\overline{v} + \overline{v}\nabla^s\right)$	$\dot{\varepsilon}_i^{\alpha\beta} = \frac{1}{2}\sum_{j=1}^{N_i}\left(\frac{m_j}{\rho_j}v_{ji}^\alpha\frac{\partial W_{ij}}{\partial x_i^\beta} + \frac{m_j}{\rho_j}v_{ji}^\beta\frac{\partial W_{ij}}{\partial x_i^\alpha}\right)$
Spin	$\overline{\overline{\Omega}} = \frac{1}{2}\left(\nabla^s\overline{v} - \overline{v}\nabla^s\right)$	$\Omega_i^{\alpha\beta} = \frac{1}{2}\sum_{j=1}^{N_i}\left(\frac{m_j}{\rho_j}v_{ji}^\alpha\frac{\partial W_{ij}}{\partial x_i^\beta} - \frac{m_j}{\rho_j}v_{ji}^\beta\frac{\partial W_{ij}}{\partial x_i^\alpha}\right)$
Conservation of energy	$\frac{\partial T}{\partial t} = \frac{1}{\rho C_p}\nabla\cdot(k\nabla T) + \dot{q}$	$\frac{\mathrm{d}T_i}{\mathrm{d}t} = \frac{1}{\rho_i C_{pi}}\sum_{j=1}^{N_i}\frac{m_j}{\rho_j}\frac{(4k_ik_j)}{(k_i+k_j)}\frac{(T_i-T_j)}{\lvert x_{ij}\rvert^2}x_{ij}\frac{\partial W_{ij}}{\partial x_i^\beta} + \dot{q}_i$

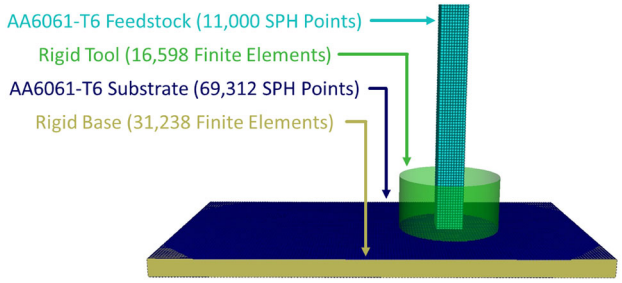

Fig. 4 SPH model of AFSD process with labeled parts used for model calibration. SPH points modeled the feedstock and substrate, and rigid finite elements modeled the tool and base

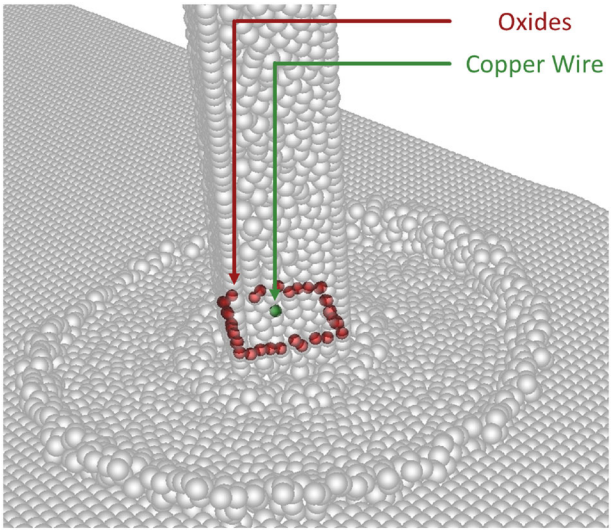

Fig. 5 SPH model of AFSD oxide and copper wire tagging for comparison with experimental AFS Depositions

spacing. Rigid finite elements were employed to reduce simulation time. For the rigid tool boundary conditions, the tool was positioned 1.5 mm over the substrate, traversed over the substrate at a fixed rate of 2.12 mm/s, and had varying rotational velocities based on the test cases (1.06 mm/s, 2.12 mm/s, 4.24 mm/s). The rigid base was fixed in space.

The thermal conductivity and heat capacity are functions that can be found in Stubblefield et al. [40]. The density was 2700 kg/m^3, the shear modulus was 26.3 GPa, and the Poisson's ratio was 0.33. The particle tracking scheme is shown in Fig. 5. SPH material points on the outer surface and center of the feedstock between 3 and 4 mm above the substrate were tagged to represent anodized oxides and copper wire, respectively. For computational efficiency of the simulations, the tagged points had the same material properties as the remainder of the AA6061-T6 feedstock. Each feedstock SPH material point had a representative diameter of 1 mm, but the oxide surface thickness on the anodized feedstock was an order of magnitude smaller at 69 μm. The main reason for this discrepancy is the computational intensity of SPH codes with available computer resources. Despite this shortcoming, the SPH model in this study is a valuable tool for predicting material flow and relative concentrations of oxides based on comparisons between experimental and computational results. Unlike the oxides, the 1 mm copper wire diameter is well represented by the 1 mm diameter SPH material points, although the copper wire would fragment into pieces smaller than 1 mm during the experimental deposition and not in the simulation deposition. Fratini et al. [45] matched FSW experiments and computer simulations using copper foil in FSW AA6082-T6. Previous studies involving both experimental and simulated tracer particles in FSW have noted that there may be a discrepancy due to the different material properties of the tracer particles relative to the rest of the material; however, studies using copper tracers in aluminum FSW have noted small differences in process parameters or negligible differences in process parameters in Schmidt et al., and that copper was successfully used as a marker material in Dickerson et al. [46, 47]. Additionally, given that copper wire had a diameter of 1 mm, and the feedstock was 9.53 × 9.53 mm^2, the copper wire only comprised 0.86% of the cross-sectional area, minimizing the impact of different material properties, compared with approximately 1.7% cross-sectional area in Schmidt et al. [47] and Dickerson et al. [47], given copper foil thickness and pin diameter.

3 Constitutive model

Due to the significant plastic deformation inherent to the AFSD process, a constitutive model is necessary for the SPH simulations. In this work, the authors employed the Fraser-Kiss-St-Georges (FKS) constitutive model, previously used for FSW simulations [38], and AFSD simulations [40]. The FKS model is laid out in Eqs. 4, 5, 6, 7, 8:

$$\sigma_y(\in^p, \in, T^*) = H(\in^p)\Lambda(\dot{\in}, T^*)\Theta(T^*) \tag{4}$$

$$H(\in^p) = a_1 + a_2 \arctan(a_3 \in^p) \tag{5}$$

$$\Lambda(\dot{\in}, T^*) = 1 + \left[b_1 T^{*b_2}\right] \ln\left(\frac{\dot{\in}}{\in_0}\right) \tag{6}$$

$$\Theta(T^*) = 1 - \frac{1}{\left(1+e^{-c_1 T^*}\right)^{\frac{1}{c_2}}} \tag{7}$$

$$T^* = \frac{T - T_{room}}{T_{melt} - T_{room}} \tag{8}$$

$H(\in^p)$ is the strain hardening parameter that depends on plastic strain $\in^p$ and fitting constants a_1, a_2, and a_3. $\Lambda(\dot{\in}, T^*)$ is the strain rate stiffening parameter that depends on homologous temperature T^*, strain rate $\dot{\in}$, reference strain rate $\dot{\in}_0$,

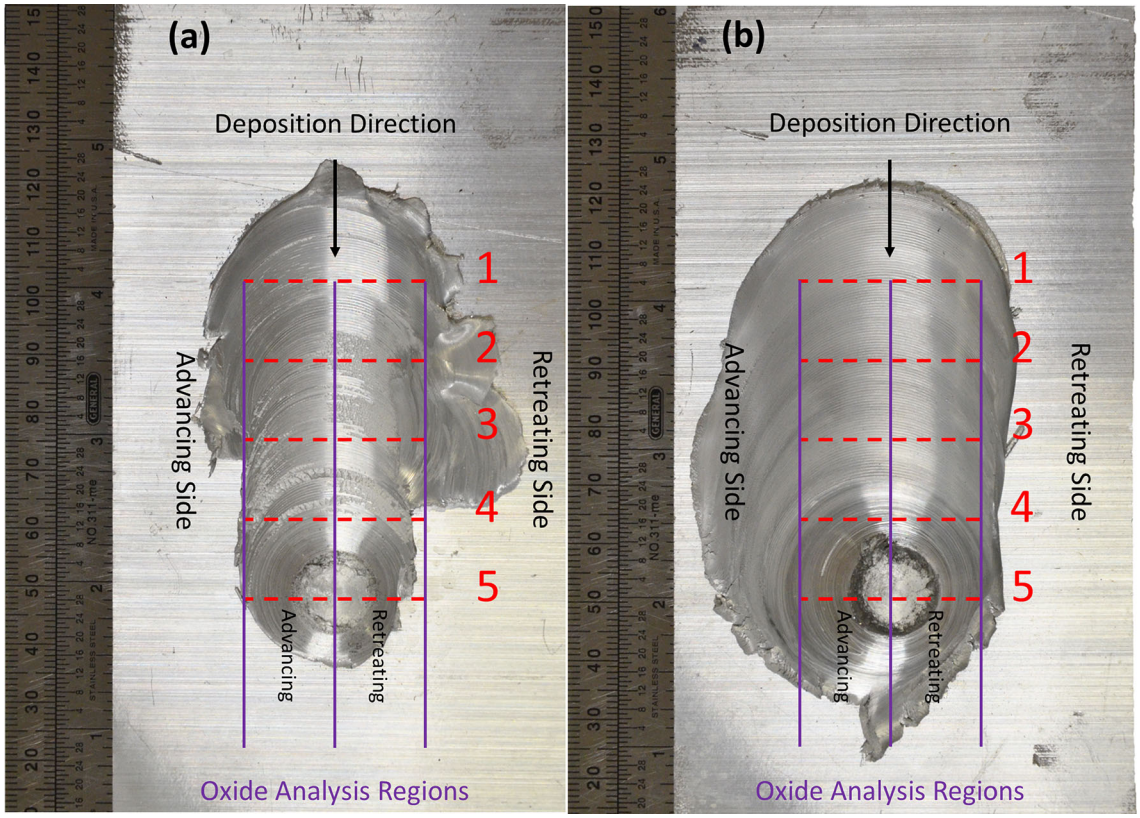

Fig. 6 **a** Starved and **b** overfed AFS Depositions created with anodized rods for model calibration with labeled oxide analysis regions. Showing oxide analysis regions used in results section

and fitting constants b_1 and b_2. $\Theta(T^*)$ is the thermal softening parameter that depends on homologous temperature T^* and fitting constants c_1 and c_2. The values for the fitting constants were taken from torsion tests in Stubblefield et al. [41] and are shown in Appendix A.

4 Results and discussion

4.1 Anodized feedstock depositions

The resulting anodized feedstock depositions with a provided schematic of the sectioned regions are shown in Fig. 6. Oxide analysis regions, marked in Fig. 6, were used to show the distribution of oxides within the depositions on the advancing and retreating sides from Regions 1–5. The advancing and retreating regions were each 15.88 mm wide. All samples were centered about the tool axis, not necessarily the center of the deposition.

The starved deposition in Fig. 6a had a significant reduction in deposition width after the start of the deposition due to inadequate material input from the low actuator feed rate. To heat up the material initially, the hollow spinning tool is brought down into contact against the substrate. Once the material is softened, the spinning tool is slowly raised up while an actuator pushes the feedstock material through the center of the tool. The deposited material fills the gap between the tool and the substrate, which is seen at the start of the deposition. However, the low actuator feed rate relative to the tool traverse speed resulted in the reduction of deposition width once the tool moves past the initial dwell zone. In contrast, the overfed deposition in Fig. 6b had a significantly wider deposition width than the starved deposition in Fig. 6a due to the high actuator feed rate. Similarly, the flash formed in Fig. 6b was thicker than the flash formed in 6a due to the higher actuator feed rate in the overfed deposition relative to the starved deposition. The overfed build in Fig. 6b showed a significant deposition bias toward the advancing side and no galling, but the starved build in 6a was more balanced and experienced significant surface galling.

ImageJ software was used to analyze the specific regions in Fig. 6. First, the images were converted to black and white via the threshold tool. Next, the particle analysis tool was employed to obtain the size of each oxide in the images. The total oxide area for advancing and retreating sides was calculated by summing oxide particle areas. A minimum oxide area threshold was varied from 1 to 1000 μm^2 to account for noise in the small specks. The oxide ratio, which is the ratio of oxide surface area on the advancing side to the retreating side, was calculated by varying the minimum oxide area

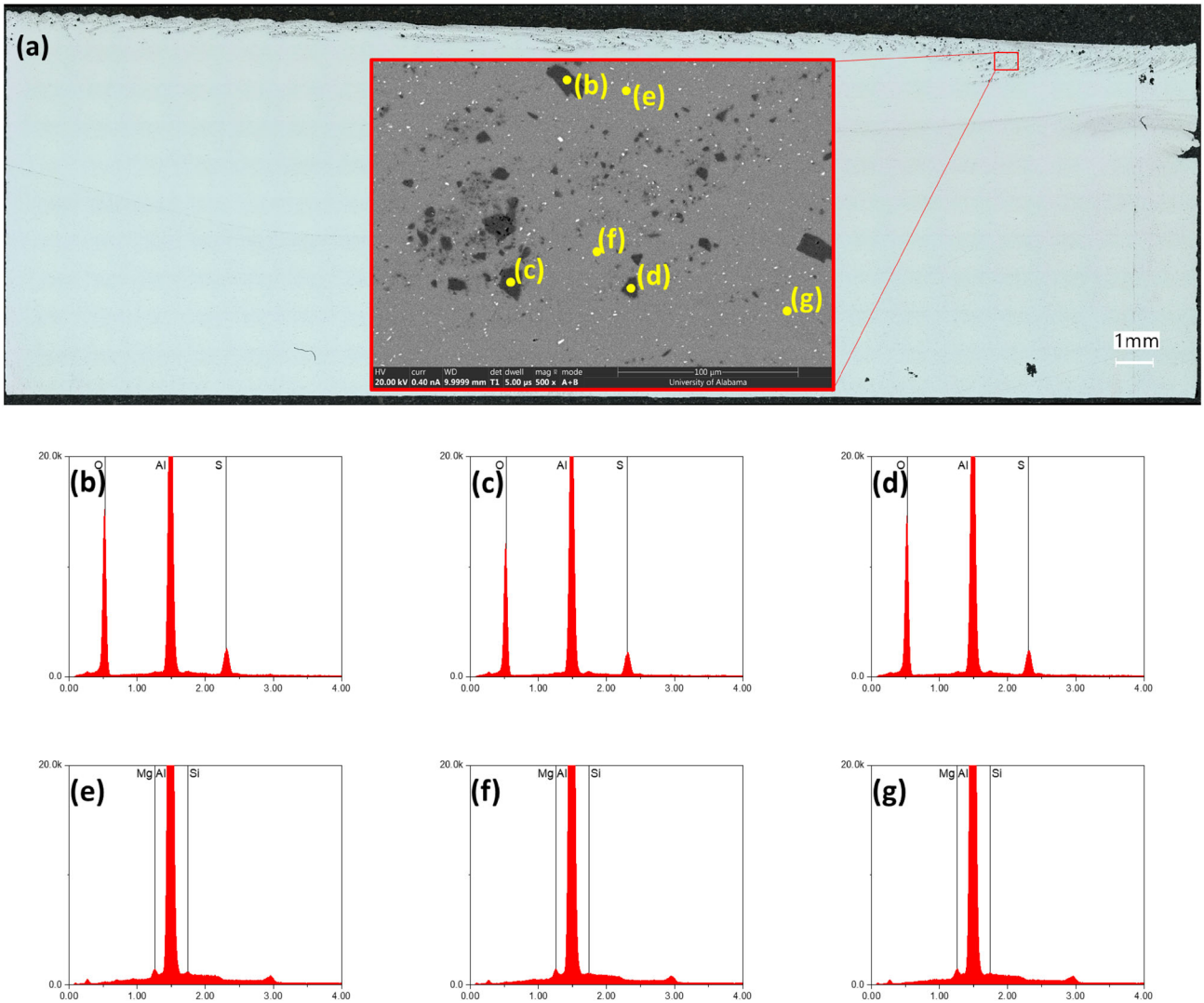

Fig. 7 **a** Region 2 micrograph of overfed anodized AFS Deposition with SEM image indicating EDS point scans. **b**–**g** EDS results from Region 2 of the overfed AFS Deposition confirm the appearance of anodized oxides

threshold and dividing the advancing side oxide area by the retreating side oxide area.

4.2 Oxide Verification

In each of the samples, dark particles visible under SEM dispersed throughout the top of the samples. In a similar study investigating the mixture of dissimilar aluminum-copper friction stir processing, Mehta et al. [48] used SEM imagery to highlight the aluminum- and copper-dense regions. The back-scattered electron image with corresponding EDS results is shown in Fig. 7. The three spots analyzed were on the dark particles, and the last three spots were analyzed on the matrix. Spots 1–3 contained significant quantities of aluminum and oxygen, indicating the presence of aluminum oxides. The presence of sulfur was a result of the anodization process, implying that spots 1–3 were aluminum oxide particles specifically from the feedstock. Spots 4–6 taken on the gray background were comprised almost entirely of aluminum, with trace amounts of other elements such as silicon and magnesium, consistent with AA6061 composition.

4.3 Anodized feedstock experiment vs simulation

The quantified experimental oxide distributions are provided in Fig. 8. Regions 1–5 on the horizontal axis correlate with the oxide analysis regions labeled in Fig. 6. The oxide ratio on the vertical axis was calculated by dividing the total oxide surface area on the advancing side by the total oxide surface area on the retreating side for each oxide analysis region in Fig. 6a,b. A high oxide ratio suggests that more oxides were found on the advancing side, and a low oxide ratio indicates that more oxides were found on the retreating side. Region 1 was

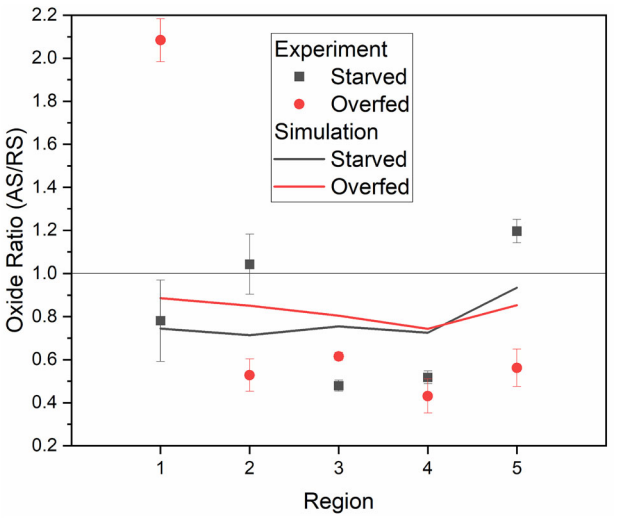

Fig. 8 Quantified AFSD oxide distributions for the anodized feedstock depositions per oxide analysis region show preference for retreating side in both **a** starved and **b** overfed builds for both experiments and simulations. The oxide analysis regions are labeled on the physical samples in Fig. 6

the start of the deposition and region 5 was the finish of the deposition. Both the starved and overfed depositions showed a low oxide ratio in Regions 2–4, indicating a preference for the retreating side in the steady-state areas. The transient areas in Regions 1 and 5 had greater variances in the oxide ratio. The discrepancy between experimental and simulated oxide distributions was anticipated and discussed in Sect. 2.4.

4.4 Copper wire core deposition

The resulting deposition with feedstock schematic is shown in Fig. 9. Since the actuator feed rate of the copper wire core deposition in Fig. 9a was between the actuator feed rates of the starved oxide deposition in Fig. 6a and overfed oxide deposition in Fig. 6b, the deposition width of the copper wire core deposition was also between the widths of the starved and overfed oxide depositions. The copper wire core deposition in Fig. 9a also experienced some flash at the start of the deposition and relatively smaller flash features on the advancing and retreating side.

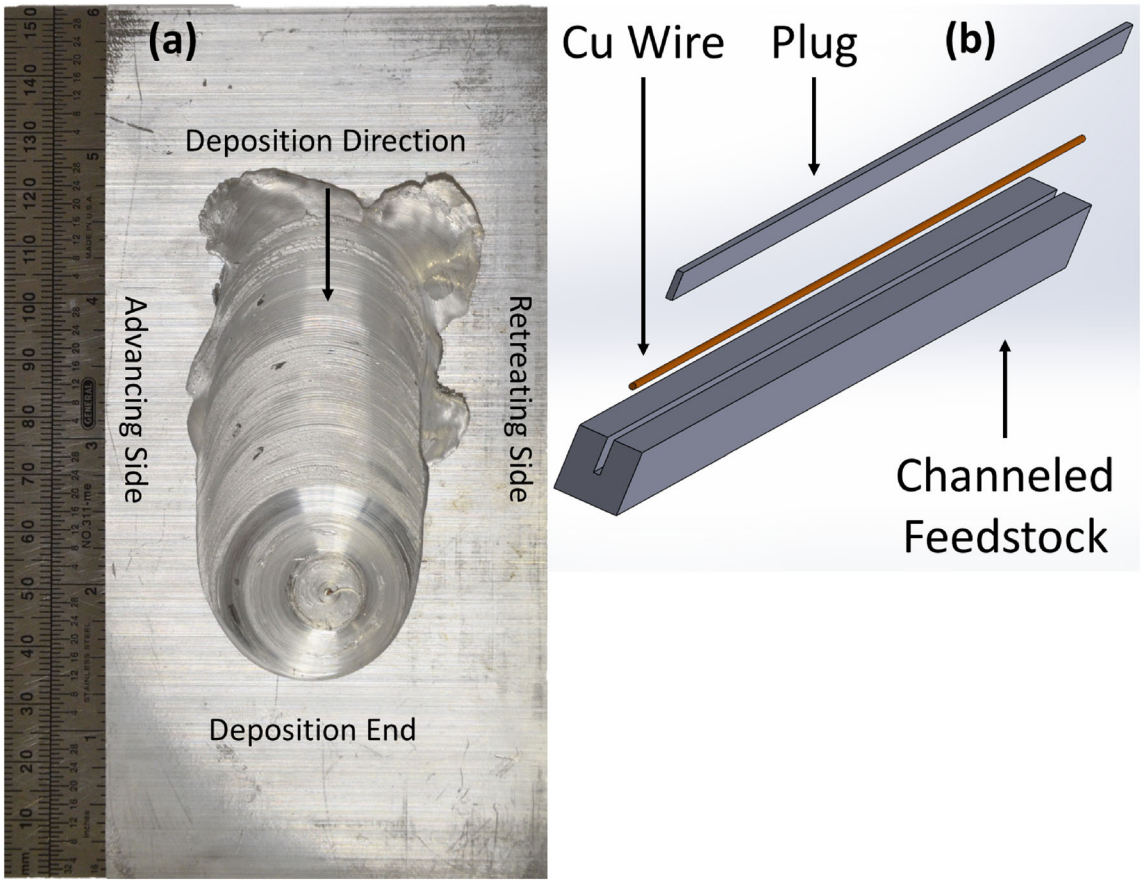

Fig. 9 **a** Copper wire core deposition using AFSD for use in SPH model calibration. **b** Schematic showing construction of copper wire core feedstock

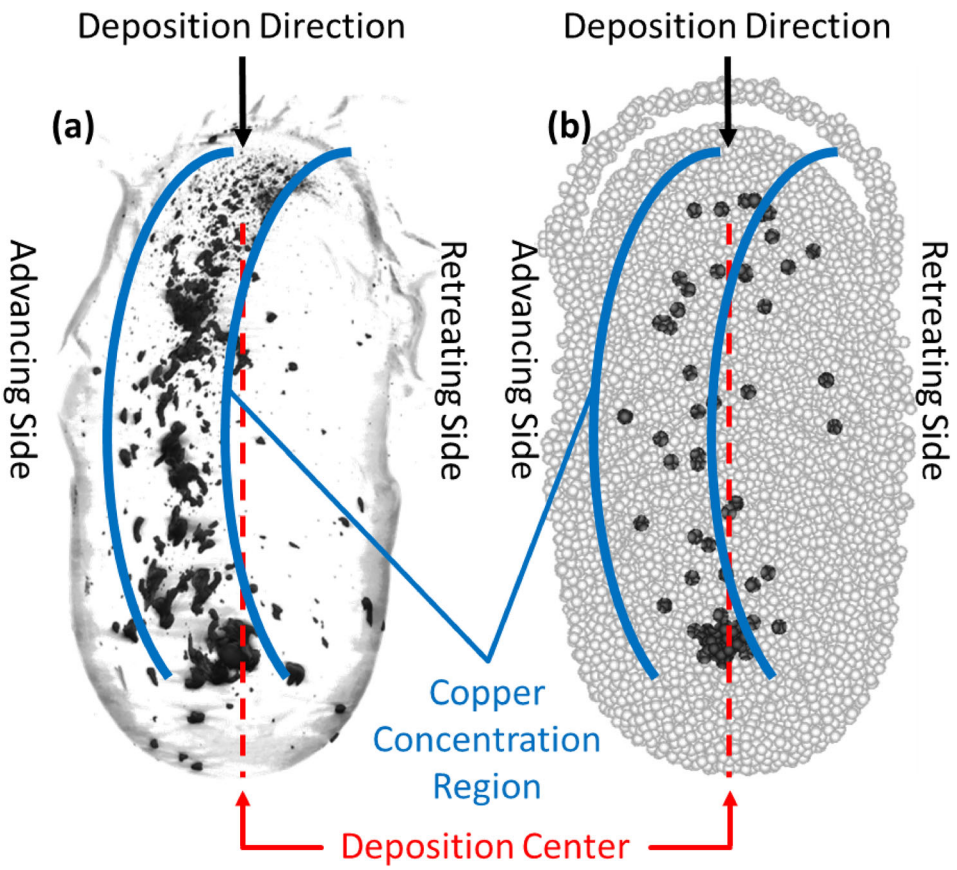

Fig. 10 **a** XRCT scan of copper wire core deposition using AFSD shows concentration of copper on the advancing side. **b** SPH simulation of AFSD process with copper wire core feedstock shows good agreement with experimental deposition

4.5 Copper wire core experiment vs simulation

The XRCT scan of the copper wire core deposition is shown in Fig. 10. The black areas are copper, and the transparent areas are aluminum. The SPH simulation in Fig. 10b shows a curved copper concentration region that correlated well with the experimental deposition in Fig. 10a. The shape of the copper concentration region was a consequence of copper fragments tending to flow to the advancing side as the copper flowed out from the center of the tool. Although the copper showed an advancing side bias, some fragments were scattered in the retreating side. A dissimilar aluminum-copper friction stir welding study by Zhou et al. [49] also showed particle fragments in the stir zone. Both the experiment and the simulation show a large cluster of copper at the end of the deposition, since the copper had not yet flowed outwards. Although the copper wire had been deformed and broken up, most of the copper wire fragments remained near other fragments, indicating a lack of material mixing. In contrast with the anodized oxides flowing to the retreating side in Fig. 8, the copper wire showed an advancing side bias in Fig. 10. This indicates a discrepancy in particle movement based on position within the feedstock, since the oxides started on the outside of the feedstock and moved to the retreating side, but the copper wire started in the center of the feedstock and moved to the advancing side.

4.6 Particle paths

4.6.1 Surface oxide particle paths

The AFSD flow behavior for the oxide particles using the tool as a fixed reference frame is shown in Fig. 11. The image in Fig. 11a shows the experimental position of the deposited particles. The vertical axis represents the tool travel direction, the horizontal axis represents the advancing and retreating sides, and the deposition direction is into the page. The feedstock rotation circumference is based on the diagonal width of the feedstock square cross section. For both Fig. 11b and c there are three competing flows that dominate different regions under the tool: (1) rotational flow, (2) radial flow, and (3) traverse flow.

Rotational flow is caused by the spin of the tool and has a significant effect while the particle is still within the feedstock rotation circumference. The reason for this flow behavior is because the force pushing down on the feedstock is greatest directly beneath the feedstock, which results in minimal slip and maximum circular movement. However, once particles moved outside the feedstock rotation circumference, the rotation flow became much weaker, due to increased slip from decreased normal forces acting on the particles. The second type of flow is radial flow, which is caused by the actuator pushing feedstock material out of the tool and onto

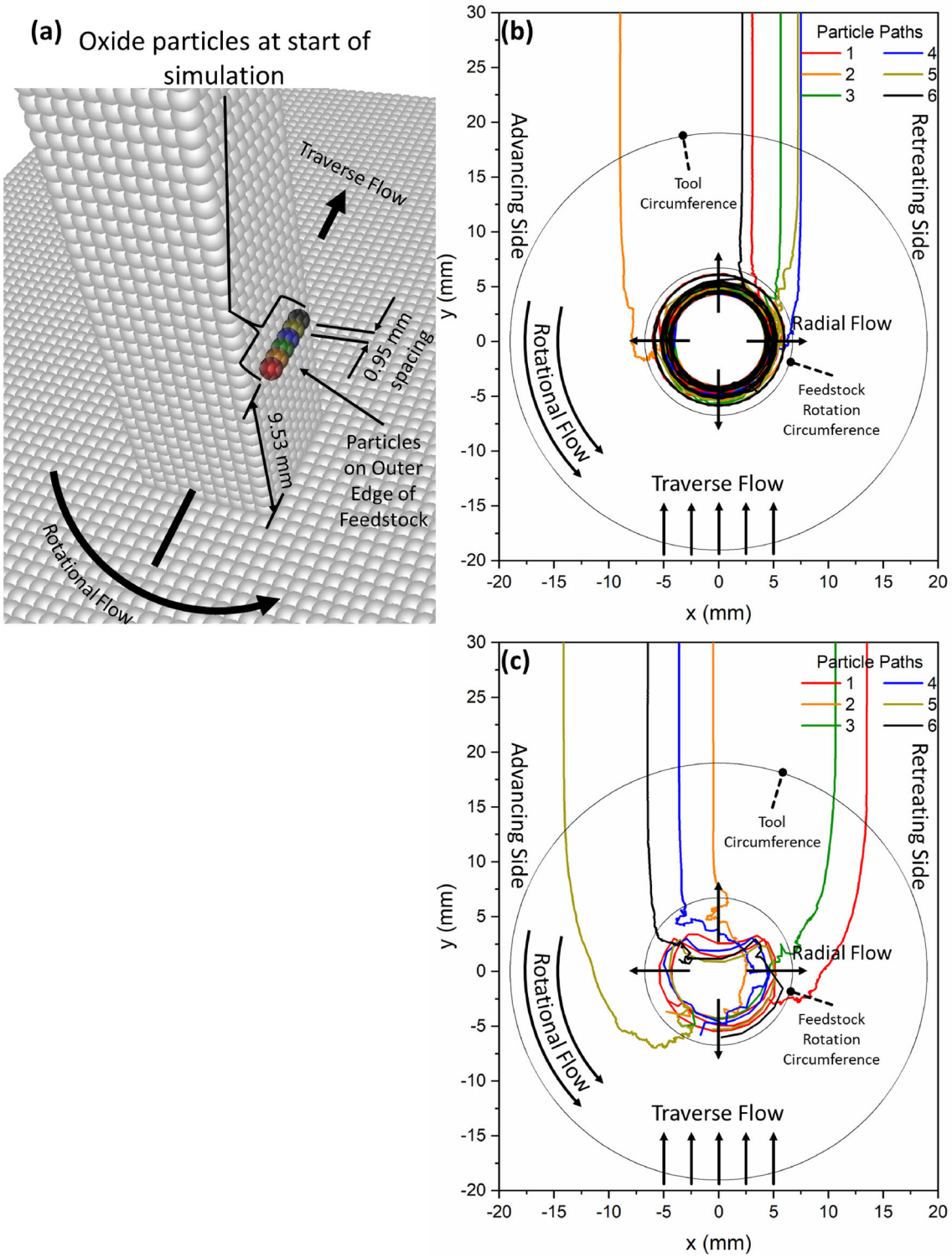

Fig. 11 **a** Location of tracked oxide particles at start of simulation on the outside of the feedstock. Oxide particle paths during **b** starved and **c** overfed simulations show three kinds of flow behaviors interact to determine particle movement: (1) rotational flow, (2) radial flow, and (3) traverse flow

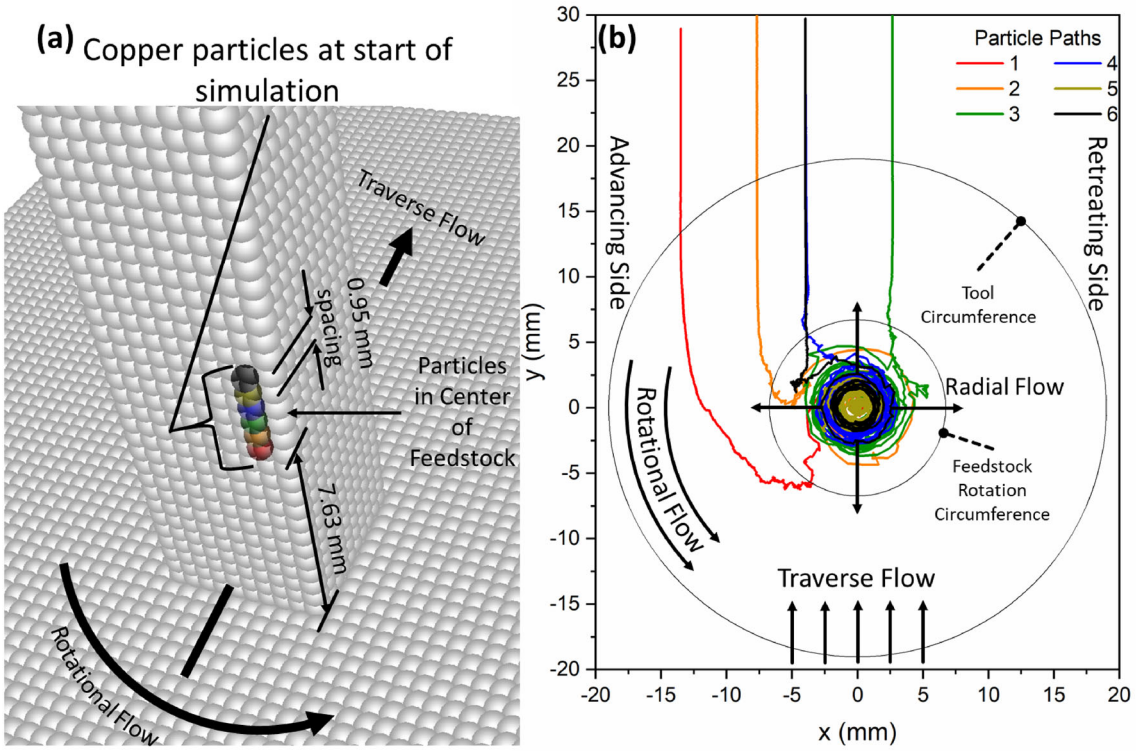

Fig. 12 **a** Location of tracked copper particles at start of simulation at the center of the feedstock. **b** The central starting position of the copper particles results in a spiral flow out of the feedstock rotation circumference

the substrate. Radial flow also occurs in FSW, as seen in Xie et al. [50]. While initially moving down the center of the tool, the radial flow shifts 90° to move parallel to the substrate away from the center of the tool. The strength of the radial flow is dependent on the actuator feed rate, which is highlighted in the different flow behaviors of the starved simulation in Fig. 11b and the overfed simulation in Fig. 11c. The overfed simulation had a significantly higher actuator feed rate than the starved simulation (4.24 mm/s vs 1.06 mm/s), which resulted in oxides in the overfed deposition flowing outwards more than oxides in the starved simulation. Also, the high radial flow of the overfed simulation in Fig. 11c interfered with the rotational flow more than in the starved simulation in Fig. 11b, which helps explain the more erratic flow behavior of the overfed simulation in Fig. 11c than the starved simulation in Fig. 11b. The third type of flow is traverse flow, which is based on the travel speed of the AFSD tool over the substrate. Unlike rotational and radial flow, traverse flow only has a significant effect once the particles are outside of the feedstock rotation circumference.

4.6.2 Internal copper particle paths

The AFSD flow behavior for the copper particles using the tool as a fixed reference frame is shown in Fig. 12. The original position of the particles is shown in Fig. 12a, which represents a section of the copper wire in the center of the feedstock shown in Fig. 9b. The vertical axis represents the tool travel direction, the horizontal axis represents the advancing and retreating sides, and the deposition direction is into the page. The feedstock rotation circumference is based on the diagonal width of the feedstock square cross section. As in Fig. 11b, c the same three flows-rotational, radial, and traverse are present in Fig. 12b. Unlike with the surface oxide particles in Fig. 11b and Fig. 11c, the copper wire particles in Fig. 7b began in the center of the feedstock and flowed outwards in a spiral pattern. Particle 5 did not escape the feedstock rotation circumference and would be present among the large cluster of copper at the end of the deposition as shown in Fig. 10.

While the anodized feedstock depositions in Fig. 8 showed a retreating side bias for oxide distribution, the copper wire core depositions in Fig. 10 showed an advancing side bias for copper distribution. This indicates that the probability of a particle to end up on the advancing or retreating side is a function of starting position in the feedstock, since the oxides in Fig. 11 were on the outer surface of the feedstock and the copper wire in Fig. 12 was at the center of the feedstock. While all particles showed the most movement within the feedstock rotation circumference, the copper particles in Fig. 12b experienced a significant drop in rotational flow while still within the feedstock rotation circumference. In

contrast, the oxide particles in Fig. 11b and c did not experience a significant drop in rotational flow until after exiting the feedstock rotation circumference.

The copper wire deposition in Fig. 10 followed the general deposition trend toward the advancing side. However, the oxides gravitated to the retreating sides of the depositions as shown in Fig. 8, despite the advancing side bias of the depositions in Fig. 6. This behavior is explained by the interaction of rotational and traverse flow. On the advancing side, the rotational flow and the traverse flow run against each other, but on the retreating side, the rotational flow and the traverse flow run with each other. This suggests that a particle is more likely ejected from the feedstock rotation circumference on the retreating side, where the net flow is the strongest, which was typically seen with the oxide particles in Fig. 8. However, for a particle starting in the center of the feedstock, the rotational flow weakens before the particle leaves the feedstock rotation circumference, because the particle is being incorporated into the deposition, which means that the traverse flow has a greater effect on particle movement. This results in the relatively stronger traverse flow pushing the particle back against the rotational flow. In this scenario, particles tend to spend more time on the advancing side where the two flows counteract each other, and therefore results in more particles that started in the center of the feedstock flowing to the advancing side. This behavior explains the bias of copper particles on the advancing side as shown in Fig. 10.

The AFSD tool used in this study has a flat shoulder face, which may explain the lack of rotational flow in Figs. 11b, c and 12b outside of the feedstock rotation circumference. Perhaps an alternate tool design such as the four-teardrop tool in [8, 12, 14] or the two-protrusion tool in [20] would encourage more flow outside of the feedstock rotation circumference. Future work could also explore different composite feedstock configurations and investigate how the constitutive elements distribute within the AFSD depositions.

5 Conclusions

In this work, a particle tracking AFSD simulation using an SPH framework was presented for the first time. Experimental depositions using two anodized AA6061-T6 rods with external oxides on the feedstock and one AA6061-T6 copper wire core feedstock were created for SPH model calibration. The anodized feedstock simulations showed a bias toward the retreating side, which reflected experimental results. The copper within the copper wire core deposition was concentrated on the advancing side with fragments dispersed throughout the deposition. The copper in the copper wire core simulation showed a similar curved copper concentration region as the experimental copper wire core deposition. The particle tracking plots indicated that particle movement was mostly limited to directly beneath the feedstock. Varying actuator feed rate influenced particle flow behavior by increasing radial flow away from the tool. Also, the particle tracking plots revealed the interaction between different material flows: rotational, radial, and traverse flow. The discrepancy between oxide particles and copper particles flowing to the retreating and advancing sides, respectively, was explained by the interaction between the different material flows.

The presented SPH model is useful for analyzing material flow within AFS Depositions, which would be time-consuming and difficult to experimentally quantify with each deposition. One advantage of having validated computer simulations of a process is the predictive power simulations provide. If defects are present at oxides, researchers can use the SPH simulations to track oxides over a battery of simulations and select optimal process parameters to push oxides to the outside of the deposition, where post-processing machining can remove the oxides. Another example involves composite feedstocks. Engineers can select optimal process parameters to ensure homogeneous mixing of different materials, without wasting resources on physical trials.

Acknowledgements A portion of this work was supported by the US Department of Defense Strategic Environmental Research and Development Program WP18-C4-1323. The authors would also like to thank the support of the US Department of Defense Science, Mathematics, and Research for Transformation Program for funding. The raw/processed data required to reproduce these findings cannot be shared at this time due to technical or time limitations.

Author Contribution GG Stubblefield contributed to formal analysis, writing—original draft, investigation, and visualization. KF contributed to investigation and writing—review and editing. NZ contributed to investigation and writing—review and editing. RPK contributed to investigation and writing—review and editing. JZT contributed to investigation and writing—review and editing. BTC contributed to investigation and writing—review and editing. J.B. Jordon contributed to funding acquisition, project administration, writing—review and editing, and conceptualization. PGA contributed to funding acquisition, project administration, writing—review and editing, and conceptualization.

Declarations

Conflict of interest The authors declare that they have no known competing financial interests or personal relationships that could have appeared to influence the work reported in this paper.

Appendix

Appendix A. Constitutive Model Constants

The FKS constitutive model constants taken from Stubblefield et al. [41] are shown in Table 2.

Table 2 FKS constitutive model constants used in this study

a_1 (MPa)	a_2 (MPa)	a_3	b_1 (MPa)	b_2	c_1	c_2
317.6	1.00	70.00	12.44	5.65	13.00	0.01

References

1. Ren SR, Ma ZY, Chen LQ (2007) Effect of welding parameters on tensile properties and fracture behavior of friction stir welded Al-Mg-Si alloy. Scr Mater 56:69–72. https://doi.org/10.1016/j.scriptamat.2006.08.054
2. He J, Ling Z, Li H (2016) Effect of tool rotational speed on residual stress, microstructure, and tensile properties of friction stir welded 6061–T6 aluminum alloy thick plate. Int J Adv Manufact Technol 84:1953–1961. https://doi.org/10.1007/s00170-015-7859-7
3. Rajakumar S, Muralidharan C, Balasubramanian V (2011) Influence of friction stir welding process and tool parameters on strength properties of AA7075-T6 aluminium alloy joints. Mater Des 32:535–549. https://doi.org/10.1016/j.matdes.2010.08.025
4. Mishra RS, Ma ZY (2014) Friction stir welding and processing II. Mater Sci Eng R 50:1–78. https://doi.org/10.1016/j.mser.2005.07.001
5. Ma ZY (2008) Friction stir processing technology: a review. Metall Mater Trans A Phys Metall Mater Sci 39A:642–658. https://doi.org/10.1007/s11661-007-9459-0
6. Nandan R, DebRoy T, Bhadeshia HKDH (2008) Recent advances in friction-stir welding - process, weldment structure and properties. Prog Mater Sci 53:980–1023. https://doi.org/10.1016/j.pmatsci.2008.05.001
7. Zhu N et al (2021) The effect of anodization on the mechanical properties of AA6061 produced by additive friction stir-deposition. Metals (Basel) 11(11):1773. https://doi.org/10.3390/met11111773
8. Phillips BJ et al (2021) Examination of parallel deposition path microstructure and material flow on interface tensile behavior for aluminum alloy Al-Mg-Si additive friction stir-deposition. J Mater Process Technol. https://doi.org/10.1016/j.jmatprotec.2021.117169
9. Avery DZ et al (2018) Fatigue behavior of solid-state additive manufactured inconel 625. J Mater. https://doi.org/10.1007/s11837-018-3114-7
10. Mason CJT et al (2021) Process-structure-property relations for as-deposited solid-state additively manufactured high-strength aluminum alloy. Addit Manuf 40:101879. https://doi.org/10.1016/j.addma.2021.101879
11. Rutherford BA et al (2020) Effect of thermomechanical processing on fatigue behavior in solid-state additive manufacturing of Al-Mg-Si alloy. Metals (Basel) 10:1–17. https://doi.org/10.3390/met10070947
12. Phillips BJ et al (2019) Microstructure-deformation relationship of additive friction stir-deposition Al–Mg–Si. Materialia (Oxf) 7:100387. https://doi.org/10.1016/J.MTLA.2019.100387
13. Avery DZ et al (2020) Influence of grain refinement and microstructure on fatigue behavior for solid-state additively manufactured Al-Zn-Mg-Cu alloy. Metall Mater Trans A Phys Metall Mater Sci 51:2778–2795. https://doi.org/10.1007/s11661-020-05746-9
14. Anderson-Wedge K et al (2021) Characterization of the fatigue behavior of additive friction stir-deposition AA2219. Int J Fatigue 142:105951
15. Yoder JK, Griffiths RJ, Yu HZ (2021) Deformation-based additive manufacturing of 7075 aluminum with wrought-like mechanical properties. Mater Des 198:109288. https://doi.org/10.1016/j.matdes.2020.109288
16. Han Y, Griffiths RJ, Yu HZ, Zhu Y (2020) Quantitative microstructure analysis for solid-state metal additive manufacturing via deep learning. J Mater Res 35(15):1936–1948. https://doi.org/10.1557/jmr.2020.120
17. Myhr OR, Børvik T, Marioara CD, Wenner S, Hopperstad OS (2020) Nanoscale modelling of combined isotropic and kinematic hardening of 6000 series aluminium alloys. Mech Mater 151:103603. https://doi.org/10.1016/j.mechmat.2020.103603
18. Schmale J, Fehrenbacher A, Shrivastava A, Pfefferkorn FE (2016) Calibration of dynamic tool-workpiece interface temperature measurement during friction stir welding. Measurement 88:331–342. https://doi.org/10.1016/j.measurement.2016.02.065
19. Perry MEJ, Griffiths RJ, Garcia D, Sietins JM, Zhu Y, Yu HZ (2020) Morphological and microstructural investigation of the non-planar interface formed in solid-state metal additive manufacturing by additive friction stir deposition. Addit Manuf 35:101293. https://doi.org/10.1016/j.addma.2020.101293
20. Griffiths RJ et al (2021) Solid-state additive manufacturing of aluminum and copper using additive friction stir deposition: process-microstructure linkages. Materialia (Oxf) 15:100967. https://doi.org/10.1016/j.mtla.2020.100967
21. Rivera OG et al (2017) Microstructures and mechanical behavior of Inconel 625 fabricated by solid-state additive manufacturing. Mater Sci Eng, A 694:1–9. https://doi.org/10.1016/j.msea.2017.03.105
22. Priedeman JL et al (2020) Microstructure development in additive friction stir-deposited Cu. Metals (Basel) 10:1538. https://doi.org/10.3390/met10111538
23. Jordon JB et al (2020) Direct recycling of machine chips through a novel solid-state additive manufacturing process. Mater Des 193:108850. https://doi.org/10.1016/j.matdes.2020.108850
24. Griffiths RJ, Petersen DT, Garcia D, Yu HZ (2019) Additive friction stir-enabled solid-state additive manufacturing for the repair of 7075 aluminum alloy. Appl Sci 9(3486):1–15. https://doi.org/10.3390/app9173486
25. Garcia D et al (2020) In situ investigation into temperature evolution and heat generation during additive friction stir deposition: a comparative study of Cu and Al-Mg-Si. Addit Manuf 34:101386. https://doi.org/10.1016/j.addma.2020.101386
26. Jordon JB, Rao H, Amaro R, Allison P (2019) Fatigue in friction stir welding. Butterworth-Heinemann. https://doi.org/10.1016/C2017-0-04065-X
27. Liu H, Ushioda K, Fujii H (2019) Elucidation of interface joining mechanism during friction stir welding through Cu/Cu-10Zn interfacial observations. Acta Mater 166:324–334. https://doi.org/10.1016/j.actamat.2019.01.004
28. Fadaeifard F, Matori KA, Abd Aziz S, Zolkarnain L (2017) Effect of the welding speed on the macrostructure, microstructure and mechanical properties of AA6061-T6 friction stir butt welds. Metals (Basel) 7:48. https://doi.org/10.3390/met7020048
29. Oosterkamp A, Oosterkamp LD, Nordeide A (2004) 'Kissing bond' phenomena in solid-state welds of aluminum alloys. Weld J 83:225–231
30. Goel P et al (2018) Investigation on the effect of tool pin profiles on mechanical and microstructural properties of friction stir butt and scarf welded aluminium alloy 6063. Metals (Basel) 8:74. https://doi.org/10.3390/met8010074
31. Li B, Shen Y, Hu W (2011) The study on defects in aluminum 2219–T6 thick butt friction stir welds with the application of multiple non-destructive testing methods. Mater Des 32:2073–2084. https://doi.org/10.1016/j.matdes.2010.11.054

32. Sato YS, Takauchi H, Park SHC, Kokawa H (2005) Characteristics of the kissing-bond in friction stir welded Al alloy 1050. Mater Sci Eng, A 405:333–338. https://doi.org/10.1016/j.msea.2005.06.008
33. Xu X, Liu Q, Qi S, Hou H, Wang J, Ren X (2021) Effect of incomplete penetration defects on mechanical and fatigue properties of friction-stir-welded 6802–T6 joint. J Market Res 15:4021–4031. https://doi.org/10.1016/J.JMRT.2021.10.028
34. Huang Y et al (2019) Microstructures and mechanical properties of micro friction stir welding (μFSW) of 6061–T4 aluminum alloy. J Market Res 8(1):1084–1091. https://doi.org/10.1016/J.JMRT.2017.10.010
35. Bin Chen H, Yan K, Lin T, Ben Chen S, Jiang CY, Zhao Y (2006) The investigation of typical welding defects for 5456 aluminum alloy friction stir welds. Mater Sci Eng A 433:64–69. https://doi.org/10.1016/j.msea.2006.06.056
36. Hamilton R, Mackenzie D, Li H (2010) Multi-physics simulation of friction stir welding process. Eng Comput (Swansea, Wales) 27(8):967–985. https://doi.org/10.1108/02644401011082980
37. Zhi Gao E, Xing Zhang X, Zhong Liu C, Yi Ma Z (2018) Numerical simulations on material flow behaviors in whole process of friction stir welding. Transact Nonferrous Metals Soc China (English Edition) 28:2324–2334. https://doi.org/10.1016/S1003-6326(18)64877-0
38. Fraser K, Kiss L, St-Georges L, Drolet D (2018) Optimization of friction stir weld joint quality using a meshfree fully-coupled thermo-mechanics approach. Metals (Basel) 8:1–24. https://doi.org/10.3390/met8020101
39. Dialami N, Cervera M, Chiumenti M, Segatori A (2019) Prediction of joint line remnant defect in friction stir welding. Int J Mech Sci 151:61–69. https://doi.org/10.1016/j.ijmecsci.2018.11.012
40. Stubblefield GG, Fraser K, Phillips BJ, Jordon JB, Allison PG (2021) A Meshfree computational framework for the numerical simulation of the solid-state additive manufacturing process, additive friction stir-deposition (AFS-D). Mater Des 202:109514. https://doi.org/10.1016/j.matdes.2021.109514
41. Stubblefield GG et al (2022) Elucidating the influence of temperature and strain rate on the mechanics of AFS-D through a combined experimental and computational approach. J Mater Process Technol 305:117593
42. Liu GR, Liu MB (2003) Smoothed particle hydrodynamics: a meshfree particle method. World Scientific Publishing. ISBN-13 978-981-238-456-0
43. Yang X, Liu M, Peng S (2014) Smoothed particle hydrodynamics modeling of viscous liquid drop without tensile instability. Comput Fluids 92:199–208. https://doi.org/10.1016/j.compfluid.2014.01.002
44. Fraser K (2017) "Robust and efficient meshfree solid thermo-mechanics simulation of friction stir welding," Université du Québec à Chicoutimi
45. Fratini L, Buffa G, Micari F, Shivpuri R (2009) On the material flow in FSW of T-joints: Influence of geometrical and tecnological parameters. Int J Adv Manuf Technol 44:570–578. https://doi.org/10.1007/s00170-008-1836-3
46. Dickerson T, Shercliff HR, Schmidt H (2003) "A weld marker technique for flow visualization in FSW," in: 4th International symposium on friction stir welding. Available: https://www.researchgate.net/publication/267224730
47. Schmidt HNB, Dickerson TL, Hattel JH (2006) Material flow in butt friction stir welds in AA2024-T3. Acta Mater 54:1199–1209. https://doi.org/10.1016/j.actamat.2005.10.052
48. Mehta K et al (2021) Investigation of exit-hole repairing on dissimilar aluminum-copper friction stir welded joints. J Market Res 13:2180–2193. https://doi.org/10.1016/j.jmrt.2021.06.019
49. Li G, Zhou L, Zhou W, Song X, Huang Y (2019) Influence of dwell time on microstructure evolution and mechanical properties of dissimilar friction stir spot welded aluminum-copper metals. J Market Res 8(3):2613–2624. https://doi.org/10.1016/j.jmrt.2019.02.015
50. Xie L et al (2022) Investigations on the material flow and the influence of the resulting texture on the tensile properties of dissimilar friction stir welded ZK60/Mg–Al–Sn–Zn joints. J Market Res 17:1716–1730. https://doi.org/10.1016/j.jmrt.2022.01.127